



A convolutional neural network -VGG16 method for corrosion inhibition of 304SS in sulfuric acid solution by timoho leaf extract

Femiana Gapsari ^{a,*}, Fitri Utaminingrum ^b, Chin Wei Lai ^c, Khairul Anam ^a, Abdul M. Sulaiman ^d, Muhamad F. Haidar ^b, Tobias S. Julian ^b, Eno E. Ebenso ^{e,f}

^a Department of Mechanical Engineering, Faculty of Engineering, Brawijaya University, MT Haryono 167, Malang, 65145, Indonesia

^b Computer Vision Research Group, Faculty of Computer Science Brawijaya University, Veteran 12-14, Malang, 65145, Indonesia

^c Nanotechnology and Catalysis Research Centre, Institute for Advanced Studies, Universiti Malaya, Level 3, Block A, Kuala Lumpur, 50603, Malaysia

^d Department of Mechanical and Industrial Engineering, Universitas Gadjah Mada, Jalan Grafika No. 2, Yogyakarta, 55281, Indonesia

^e Centre for Materials Science, College of Science, Engineering and Technology, University of South Africa, Johannesburg, 1710, South Africa

^f Institute for Nanotechnology and Water Sustainability, College of Science, Engineering and Technology, University of South Africa, Johannesburg, 1710, South Africa



ARTICLE INFO

Keywords:

Convolutional neural network (CNN)

Corrosion inhibitor

Machine learning

Timoho leaf extract

VGG16

ABSTRACT

A corrosion inhibition test, coupled with a quantification of in-situ H_2 evolution, can be used to evaluate an organic inhibitor such as Timoho leaf extract (TLE). TLE is a biodegradable and effective corrosion inhibitor because of its potential to protect 304SS against sulfuric acid. TLE corrosion inhibitor was studied through systematic electrochemical experiments and morphological characterization, with a concentration range of 0–6 g L^{-1} . Convolutional Neural Network (CNN)-VGG16 was one of the machine learning approaches used to classify and predict physical changes in hydrogen gas bubbles. Constituents of the TLE and 304SS surfaces were analyzed by FT-IR and UV-Vis tests. The results suggested that 3 g L^{-1} TLE inhibitor was able to reduce the corrosion rate by 99.37 %. The TLE's inhibition mechanism on 304SS was mixed adsorption and mixed type inhibitor that followed the Isothermal Freundlich Equation. The prediction model by CNN-VGG16 for corrosion tests at varied inhibitor doses was 96% accurate. SEM tests revealed that TLE constituent adsorption on the 304SS surface had a smooth surface morphology with few degraded spots.

1. Introduction

Stainless steels are utilized in the oil and petrochemical industry, particularly in desalination plants [1]. They exhibit remarkable corrosion resistance, but their use in plants has evolved with the introduction of high-alloy stainless steels, which offer enhanced resistance to concentrated acid [2,3]. The presence of calcium and magnesium-based deposits in desalination plants cannot be avoided. Acids such as sulfamic acid (HSO_3NH_2), hydrochloric acid (HCl) and sulfuric acid (H_2SO_4) are employed to dissolve such deposits [1]. Sulfuric acid is one of the most commonly utilized acids in solution form [4,5]. In all sulfuric acid concentrations and temperatures, the corrosion mechanism of 304SS involves the spontaneous active-passive transition at anodic potentials [6,7]. Sulfuric acid oxidizes at high concentrations and reduces at low concentrations. Therefore, the corrosion mechanism is expected to change when alloys are exposed to varied acid concentrations [8].

Acid corrosion inhibitors, such as organic compounds with high

electron density, are employed to mitigate material loss that may occur upon contact with acid. They effectively reduce material loss [4]. Synthetic inhibitors are toxic, but eco-friendly compounds offer superior corrosion protection due to their eco-friendliness, biodegradability, and availability, making them a promising alternative to synthetic inhibitors [9,10]. Organic compounds which have a long aliphatic chain are the most prevalent corrosion inhibitors [4,11]. The increase in side chains within a functional group leads to a rise in the hydrophobic nature of organic compounds, thereby increasing their toxicity [12]. Double or triple bonds in molecules offer corrosion inhibition benefits, but they also increase toxicity [4]. Due to their non-toxicity, nature-friendly behavior, and economical and renewable qualities, plant extracts have recently gained favor as organic corrosion inhibitors. Generally, organic inhibitors contain O, N, and S atoms and double bonds [13,14]. Restricted plants are utilized as the main substrates for the development of botanical extracts, which are essential for the production of corrosion inhibitors. Nature-derived organic inhibitors are usually obtained from

* Corresponding author.

E-mail address: memi_kencrut@ub.ac.id (F. Gapsari).

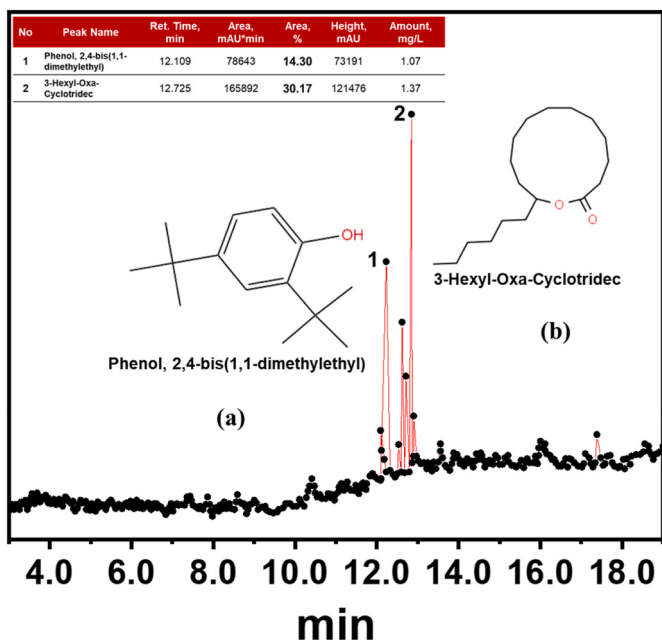


Fig. 1. The molecular structure of the phytochemicals constituting TLE, (a) Phenol and (b) Cyclotridec.

parts of botanical components, such as leaf extract [15–18], tree bark [19,20], seed [21], fruit [22–24] and trunk [25,26]. These substances have been proven to be effective in inhibiting corrosion.

Corrosion rate test is classified into long-term and short-time tests. Short-term test is usually performed by electrochemical methods [27]. The issue is that short-term testing does not reflect long-term corrosion. Similarly, long-term corrosion testing requires constant test duration and conditions as used in short-term testing. Corrosion rate and hydrogen evolution are not visible in real time [28]. Therefore, it is necessary to perform a test combination of long-term and short-term tests to examine any physical change during the corrosion process and inhibitor addition. Machine learning has significantly enhanced the efficiency of planning and execution of physical change monitoring and inspection tasks [29,30]. Deep convolutional neural networks (CNN) are widely utilized in computer vision, image categorization, and object recognition [30]. One of the reliable CNN methods for classification and detection is VGG16. VGG16, a CNN-based system, excels in image classification by reliably identifying large datasets using transfer learning techniques and accurately extracting high-level features from images [31]. For this reason, physical changes on metal surfaces in the presence of corrosion inhibitors are classified with CNN-VGG16.

Research on the use of organic inhibitors for steel has been widely conducted. Studies have been carried out to look for sustainable alternative organic inhibitors which are abundantly available in nature. This study used Timoho leaf extract (TLE) as an organic inhibitor. The research on the Timoho plant addresses the issue of extracting maximum plant materials from medicinal and food-producing plants. The use of TLE aims to increase the use value of abundant and unutilized timoho leaf waste. In Indonesia, Timoho leaves are not much used compared to the roots, bark and stems. Timoho fiber obtained from the bark has been proven to be able to be used in fiber and nanocellulose in composites [32–34]. Timoho leaves need to be utilized more, so they are not wasted. The Timoho leave waste can be used as an organic inhibitor in steel [35, 36]. The content in Timoho leaves is almost the same as in the stem and roots and is very potential as a corrosion inhibitor. TLE has been studied for its ability to inhibit 304SS corrosion in 0.5 M H₂SO₄. The prediction of hydrogen gas bubbles on 304SS surfaces was conducted using a CNN-VGG16. The electrochemical method was performed for the corrosion test. The effect of inhibitor variation on the inhibition

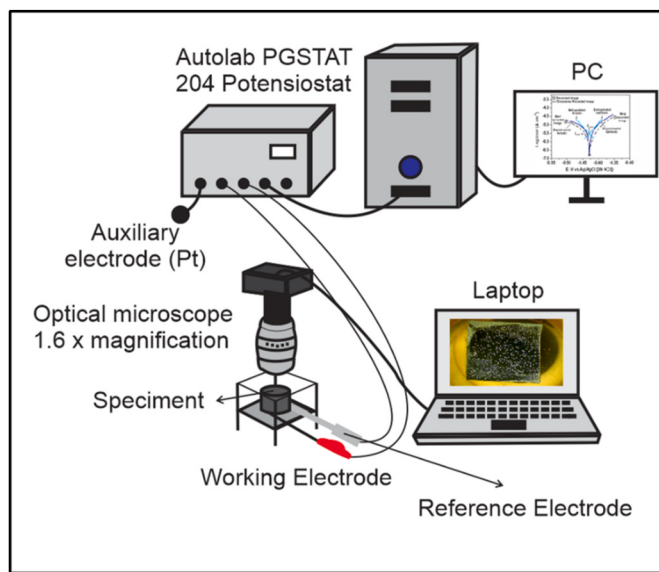


Fig. 2. The electrochemical data and image capture setup were utilized in the experiment.

efficiency and mechanism is also discussed in this study.

2. Material and methods

304SS was used with chemical composition (% weight) of 0.07 C, 8.14 Ni, 18.2 Cr 0.9 Mn, 0.53 Si 0.035 P, 0.017 S, Bal. Fe. TLE inhibitor was isolated from Timoho leaves and prepared by oven-drying wet 2000 g Timoho leaves at 40 °C, crushing the leaves into powder, and macerating the powder for 80 h at 25 °C in an ethanol solvent. Then, the leaves mixture was filtered and evaporated to get a thick extract. The identification of chemical compounds and extract material was conducted using a Fourier-Transform Infrared (FTIR) Spectrometer (Spectrum Two, PerkinElmer, Buckinghamshire, UK) and a Gas Chromatography Mass Spectrometer (GCMS, PerkinElmer, UK). The gas chromatography-mass spectrometry (GCMS) study indicated that the tested liquid extract (TLE) primarily consisted of phenol and cyclotridec. The molecular structure present in TLE is illustrated in Fig. 1. Absorbance measurement was conducted using Ultraviolet-visible (UV-VIS) type AMV11 AMTAST and measured at wavelengths of 200–800 nm.

One batch of sulfuric acid (H₂SO₄) of 0.5 M was filled with varied concentrations of TLE. 0, 1, 2, 3, 4, 5, and 6 g L⁻¹ of TLE inhibitor were added. The testing was performed at a room temperature of 298 K. Electrochemical testing was conducted using Autolab PGSTAT 128 N. The specimen that had been obtained was incorporated into an electrochemical cell, wherein a reference electrode consisting of Ag/AgCl (KCl 3 M) was utilized alongside a platinum auxiliary electrode. The three electrodes were submerged in the solution for 30 min. Polarization was measured at changes of -0.1 to +0.1 V along the corrosion potential (OCP) with a scan rate of 0.001 V/s. The calculation of inhibition efficiency was performed utilizing Equation. (1) [37–39]:

$$IE (\%) = \frac{i_{corr} - i_{corr(i)}}{i_{corr}} \times 100 \quad (1)$$

The corrosion current density in corrosion media without and with inhibitor is represented by the i_{corr} and $i_{corr(i)}$. OCP measurement was done prior to the tafel polarization test. The specimen was immersed in 0.5 M sulfuric acid for 30 min to achieve OCP potential stability.

The measurement of electrochemical impedance spectroscopy (EIS) was conducted at a frequency of 10⁵–0.1 Hz with an amplitude of 10 mV peak to peak and AC signal at OCP. The inhibition efficiency was determined by the EIS method and formulated in Equation (2) [26]:

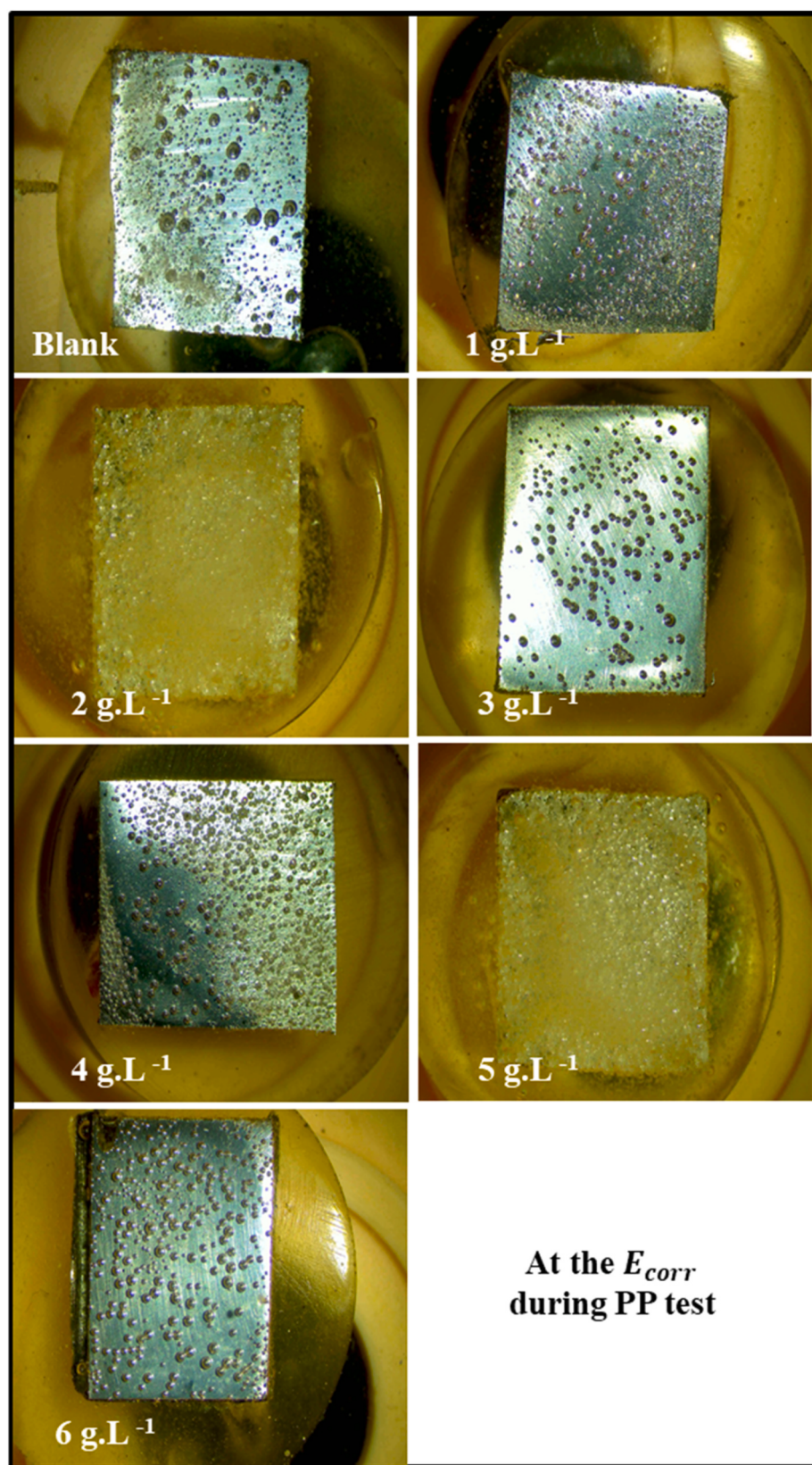


Fig. 3. Visualization of data distribution of the training set.

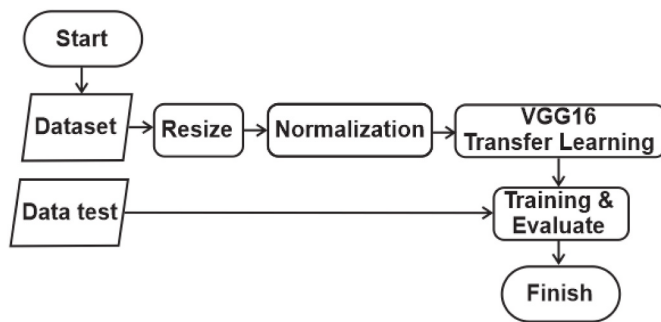


Fig. 4. Block diagram.

$$\text{IE (\%)} = \frac{R_p - R_{p(i)}}{R_p} \times 100 \quad (2)$$

The R_p and $R_{p(i)}$ reflect the polarization resistance in corrosion media with and without TLE inhibitor addition.

2.1. Data modelling

In this study, data were used in the form of images consisting of 3003 images in JPG format. They come from 7 different datasets, namely metals with additional solutions of blank, 1, 2, 3, 4, 5, and 6 g L⁻¹. The data collection procedure is shown in Fig. 2.

The objects studied in the research were images of hydrogen bubbles. The image data consist of 70% training data and 30% validation data. Fig. 3 was the visualization of data distribution of the training set and test set on each label.

The VGG16 deep learning method was employed in the system design to detect gas bubbles on the surface of the 304SS. The system block diagram in the study has three parts namely the input, processor, and output (Fig. 4). The dataset is a part of the input. Next, the dataset was fed into the processing section which started with the preprocessing process of resizing the images to 150 x 150 pixels. The next stage was to classify the image dataset into training and validation datasets with successive configurations of 70 and 20%. The training and validation datasets were used as input in the VGG16 classification model training process. The output of the VGG16 classification was the system output of 7 304SS surface classes added with blank, 1, 2, 3, 4, 5, and 6 g L⁻¹.

Before the dataset was used in the training phase, multiple augmentations were applied to the data to increase the amount of data used for the training model and prevent overfitting. Training dataset augmentation was done by using Roboflow with several parameters, namely inverting the image, distorting the image ($\pm 4^\circ$ horizontally and $\pm 5^\circ$ vertically), changing the image saturation (between -33 and +33%), and altering the exposure of the image (between -15 and

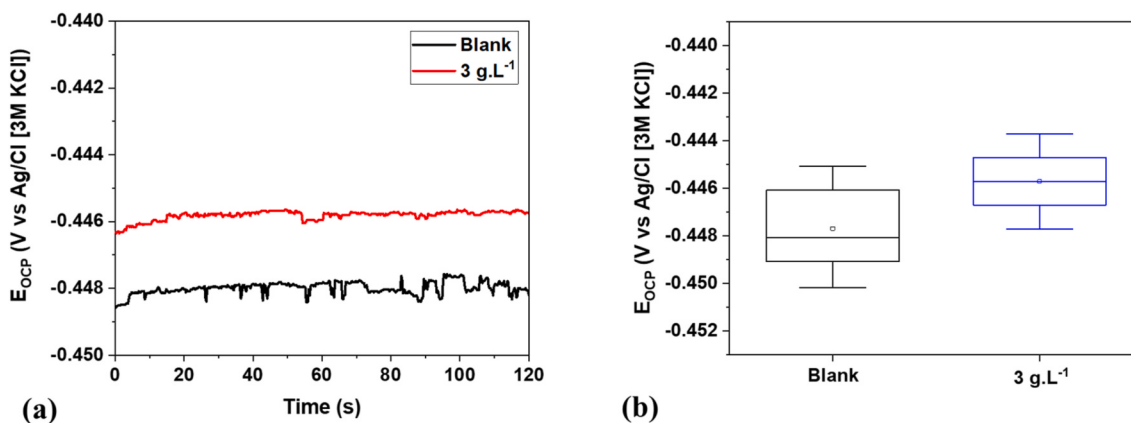
+15%). The dataset was also subjected to a data generator process provided by hardware with several parameters: rotation ($0\text{--}45^\circ$), distortion (with 0.1 intensity), zooming (between +0.1 and -0.1), flipping horizontally, and filling the empty parts of the image due to augmentation. After all data were subjected augmentation process, they were used to train the VGG16 model. The training process used the VGG16 weighting that had been pre-trained in imageNet dataset. However, all layers on VGG16 would be trained further in the training process. Following VGG16, some dense layers and dropouts were employed. The training was performed using the Adam optimizer which was utilized with a learning rate of 0.0001, a batch size of 16, and a total of 8 epochs.

Model testing involved evaluating the achievement of models that had been trained to predict several images that had been separated as a test set, which represented 10% of the images in the dataset. Unlike data in the training process, the data used for testing were raw data without any augmentation. Additionally, the data had been isolated from the start so that they were not included in the training process. The results of the model testing can be seen in the confusion matrix which maps the input and the prediction results as well.

2.2. Quantum chemistry

Density functional theory (DFT) with a B3LYP theory level approach on DFT and base set of electrons 6-31G (d) on all atoms were applied to analyze quantum chemistry. All the quantum chemistry processes done used Orca 5.0.3 application to facilitate the molecule structure optimization, obtain quantum chemistry parameters such as E_{HOMO}, E_{LUMO}, E_{LUMO}-E_{HOMO} (ΔE), total energy and Mulliken charge in heteroatoms (N, O, and S), and get the analysis. The electrostatic potential was determined by operating the Gaussian 09 and Gausview 6.0.16 applications. The quantum analysis concludes that structural geometry optimization is used to find the physical properties of TLE inhibitors. Parameters such as nucleophilicity (ϵ), hardness (η), softness (σ), electronegativity (χ), electrophilicity index (ω), and chemical potential (μ), serve as indicators for the stability, reactivity, and strength of inhibitor adsorption.

The quantum chemical study was carried out by analyzing the main components of phenol in TLE using the density functional theory (DFT) method. B3LYP theory-level approach in DFT with a 6-31G(d) electron basis set on all atoms was defined using the Gaussian 09 RevD.01 application. The present methodology was employed to assess the influence of molecular structure and electronic characteristics on the suppression of the corrosion. The production of molecular structure and the optimization of geometry were carried out using the software applications ChemDraw Ultra 12 and Avogadro, respectively. HOMO and LUMO analysis employed Gaussview 6.0.16. These applications were used to analyze molecular structure optimization and obtain quantum chemical parameters. The parameters follow equations (3)–(9):

Fig. 5. The OCP curve of the Tafel polarization test, a) typical OCP curves for the specimens immersed in 0.5H₂SO₄ (b) measured OCP values.

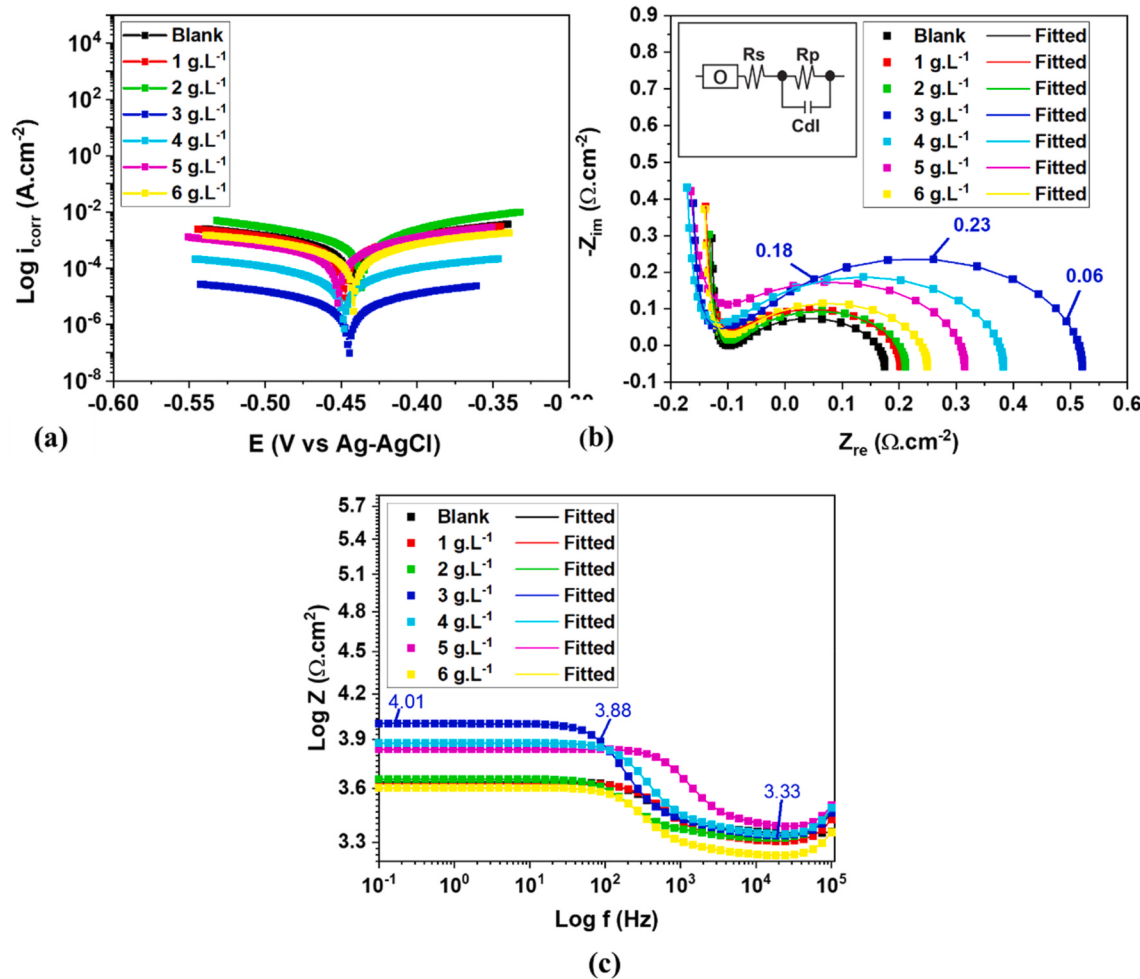


Fig. 6. The results of the electrochemical test (a) tafel plots (b) EIS curve (c) bode plot with TLE concentration variations.

$$\mu = -\chi = \left(\frac{\partial E}{\partial N} \right)$$

$$(3) \quad \eta = \frac{I + A}{2} \quad (6)$$

$$\eta = \frac{1}{2} \left(\frac{\partial^2 E}{\partial N^2} \right) = \frac{1}{2} \left(\frac{\partial \mu}{\partial N} \right)$$

$$(4) \quad \sigma = \frac{1}{\eta} \quad (7)$$

$$\chi = -\mu = \left(\frac{I + A}{2} \right)$$

$$(5) \quad \chi = -\mu = \left(\frac{-E_{HOMO} - E_{LUMO}}{2} \right) \quad (8)$$

$$(9) \quad \eta = \left(\frac{E_{LUMO} - E_{HOMO}}{2} \right)$$

Table 1

The polarization parameters of 304SS in 0.5 M H₂SO₄ at various concentrations of TLE.

Variation (g.L ⁻¹)	β_a (V/dec)	$-\beta_c$ (V/dec)	E_{corr} (V)	i_{corr} (x 10 ⁻³ A/cm ²)	Corrosion rate (mm/year)	IE (%)
Blank	0.31 ± 0.02	0.32 ± 0.02	0.44 ± 0.01	3.57 ± 0.51	41.53 ± 2.42	–
1	0.38 ± 0.03	0.27 ± 0.05	-0.44 ± 0.03	1.81 ± 0.41	21.06 ± 1.82	45
2	0.15 ± 0.04	0.08 ± 0.02	-0.43 ± 0.02	1.18 ± 0.34	13.66 ± 1.13	61
3	0.35 ± 0.04	0.38 ± 0.01	-0.44 ± 0.04	2.22 ± 0.28	0.25 ± 0.06	99
4	0.35 ± 0.02	0.36 ± 0.03	-0.45 ± 0.01	178 ± 0.30	2.07 ± 0.09	97
5	0.87 ± 0.07	0.17 ± 0.04	-0.45 ± 0.03	1.69 ± 0.40	19.65 ± 2.03	47
6	0.92 ± 0.06	0.50 ± 0.03	-0.44 ± 0.03	2.31 ± 0.50	26.86 ± 2.4	31

The ionization energy (I) and electron affinity (A) of the investigated molecules are determined with the HOMO and LUMO energies.

3. Results and discussion

3.1. OCP analysis

The OCP measurement at each time at room temperature is demonstrated in Fig. 5. Fig. 5 also displays the curves of the time (t) and potential difference (E_{OCP}) of 304SS in 0.5H₂SO₄ with and without a TLE inhibitor. The OCP characteristics of 304SS are different. Although the two curves in the potential axis shift, their shapes are alike [40]. Despite the significant variation in the EOCP values seen among different point pairs, there is a consistent similarity in the difference between the initial potential and the asymptotic value, denoted as E_∞ , as time progresses.

In the OCP test, during 120 min, the variation without the inhibitor

Table 2

Isothermal adsorption and thermodynamic parameters for 304SS in 0.5H₂SO₄ presence and absence of TLE inhibitor.

Adsorption equation	Linear equation	Kads	ΔG_{ads} (kJ/mol)
Isothermal Langmuir	$y = 0.66x + 1.41$	0.71	- 9.20
Isothermal Freundlich	$y = 0.53x - 0.31$	2.04	- 11.85
Isothermal Temkin	$y = -0.44x - 0.13$	1.35	- 10.81
Isothermal Frumkin	$y = 2.92x - 1.67$	46.77	- 19.70

(Fig. 5b) is seen to have a higher fluctuation than that of the variation with the 3 g L⁻¹ inhibitor. The OCP value and fluctuation can affect the hydrogen evolution, which generally appears in electrolyte solution as bubbles. The bubbles expand rapidly and are detached from the specimen's surface [41]. The 3 g L⁻¹ inhibitor presents a higher OCP value than the unimmersed inhibitor. This means the presence of different anodic and/or cathodic kinetics and more positive OCP values which can be attributed to the low hydrogen evolution rate behavior and hydrogen rate aligned with the corrosion rate in the polarization test [40].

3.2. Tafel polarization

Fig. 6a shows the Tafel plot of 304SS at varied TLE inhibitor concentrations in 0.5 M H₂SO₄.

The use of a TLE concentration of 3 g L⁻¹ resulted in the lowest corrosion rate of 0.25 mm/year and the maximum inhibition efficiency of 99% (Table 1). The findings suggested that the addition of the inhibitor at concentrations of up to 3 g L⁻¹ substantially reduced the corrosion rate of 304SS. The rise in IE % values was in line with the

decrease in corrosion current density (i_{corr}). The corrosion rate, directly linked to the i_{corr} , decreased with the introduction of a TLE inhibitor at concentrations of 1–3 g L⁻¹, increasing with concentrations of 4–6 g L⁻¹. The corrosion rate was found to be the lowest at a concentration of 3 g L⁻¹. This can be attributed to the presence of the inhibitor molecules which were evenly distributed on the surface of the metal, effectively retarding the corrosion process [42].

The optimum inhibition efficiency occurred at 3 g L⁻¹ addition and dropped with the increase in inhibitor concentration. This was probably due to the physical adsorption mechanism. The TLE inhibitor demonstrated an optimal concentration of 3 g L⁻¹. When exceeding this concentration, the inhibitor reached saturation or detached from the created layer. This phenomenon can be attributed to the enhanced intermolecular interactions compared to the interactions between the inhibitor and the metal surfaces [43]. The addition of TLE inhibitor beyond 3 g L⁻¹ weakened the protective layer formed on the surface of 304 SS.

The anodic Tafel constant (β_a) is associated with the adsorption of inhibitor molecules on the anodic side. In contrast, the cathodic Tafel constant (β_c) is linked to the hydrogen evolution reaction occurring at the cathodic electrode. The TLE inhibitor addition shifts the anodic and cathodic sections in the Tafel plot (Fig. 6a). The shift reduces the corrosion rate density in all tested concentrations and decreases the corrosion rate significantly. The shift of cathodic and anodic branches in the Tafel plot indicates that there is a cathodic and anodic mixed reaction. The results of the study reveal that TLE inhibitor addition has shifted the E_{corr} to a more negative or positive value. However, the shift is not significantly obvious. The data shown in Fig. 6a and Table 1 indicate that the observed alterations in E_{corr} values are consistently below 85 mV. Therefore, it may be argued that TLE functions as a mixed-

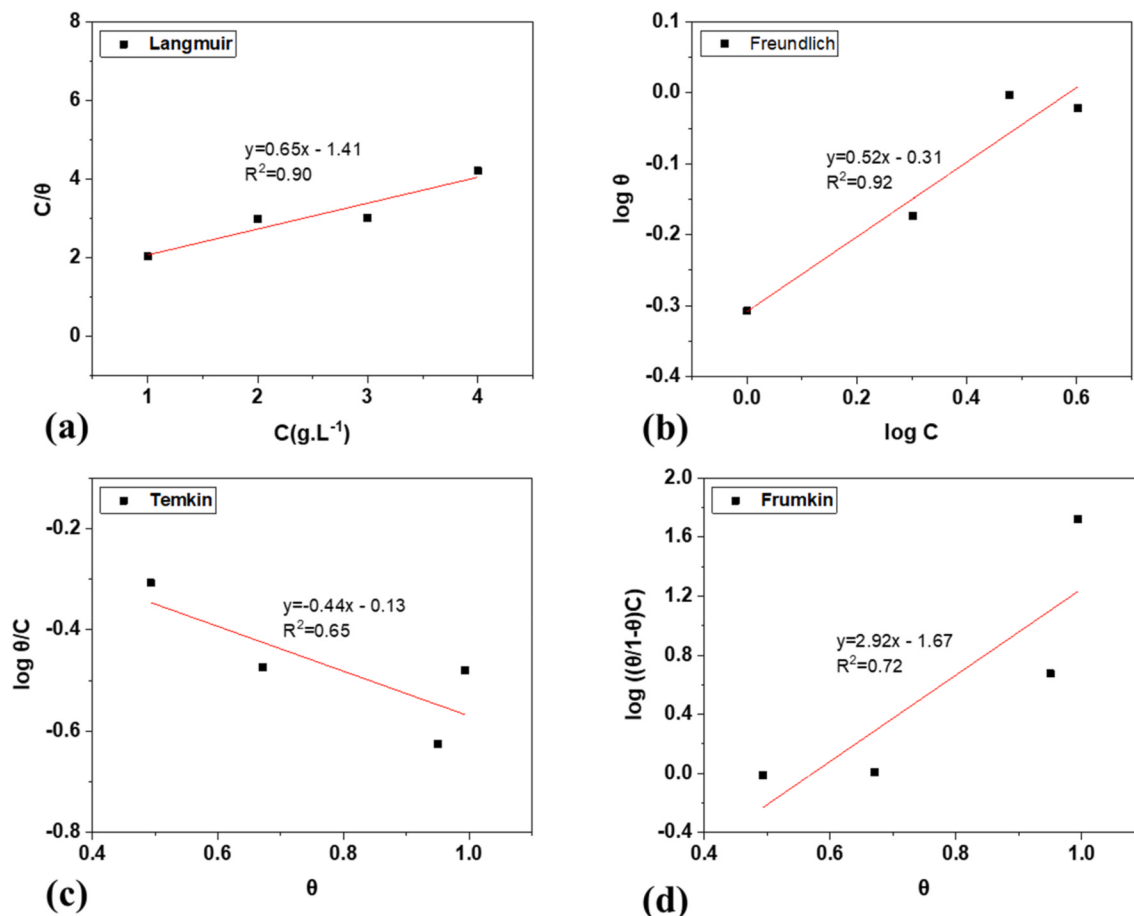


Fig. 7. a) Langmuir , b) Freundlich , c) Temkin , d) Frumkin Adsorption Isotherm of 304SS

Table 3
Impedance parameters of 304SS in 0.5 M H₂SO₄.

Variation (g. L ⁻¹)	O (F. cm ²)	Rs (Ω. cm ²)	Rp (Ω. cm ²)	Cdl (x 10 ⁻⁸ F/ cm ²)	χ^2	IE (%)
Blank	0.10 ± 0.04	3.32 ± 0.02	139.5 ± 32	5.22 ± 0.21	0.18 ± 0.01	–
1	0.07 ± 0.01	3.23 ± 0.03	253.2 ± 26	8.93 ± 0.11	0.05 ± 0.02	45
2	0.12 ± 0.03	3.16 ± 0.06	381.8 ± 37	9.01 ± 0.15	0.08 ± 0.01	63
3	0.06 ± 0.02	3.04 ± 0.05	788.9 ± 37	9.01 ± 0.13	0.08 ± 0.02	82
4	0.05 ± 0.01	3.21 ± 0.03	698.6 ± 29	9.01 ± 0.21	0.07 ± 0.02	80
5	0.03 ± 0.01	3.20 ± 0.04	362.9 ± 27	8.56 ± 0.12	0.26 ± 0.01	61
6	0.08 ± 0.02	3.14 ± 0.03	234.8 ± 31	9.01 ± 0.22	0.04 ± 0.01	40

type inhibitor, exerting influence over both the cathodic and anodic reactions when added to a 0.5 M H₂SO₄ solution. The morphologies of tafel plots, both with and without the presence of an inhibitor, exhibit a high degree of similarity. This finding suggests that the corrosion of 304SS was impeded by the adsorption of organic molecules present in TLE. These compounds block the reaction site but do not change the anodic and cathodic corrosion reaction mechanisms [44–46]. The inhibitor addition to all concentrations contributes to the significant decrease in i_{corr} in 0.5 M H₂SO₄. This indicates the formation of the TLE organic molecules inhibiting film on the surface of 304SS and the value of efficiency and inhibition effects.

3.3. Adsorption isotherm of TLE

Fig. 7 illustrates the adsorption isotherm of 304SS in a 0.5H₂SO₄ solution, both with and without the addition of a TLE inhibitor.

Adsorption of organic molecules can inhibit metal corrosion, influenced by the molecules' chemical composition and the metal's electrochemical potential, as demonstrated through isothermal adsorption experiments. In this study, the adsorption isotherm analysis was modified to incorporate several isothermal equations, including Frumkin, Langmuir, Temkin, Freundlich (Table 2). The study's most optimal outcomes adhere to the Freundlich adsorption isotherm equation. (Equation (10)).

$$\text{Freundlich equation : } \log \theta = \log K_{ads} + n \log C \quad (10)$$

The analysis of the Freundlich adsorption isotherm was conducted to understand the fundamental interaction between the inhibitor and the surface of 304SS. The process of adsorption of inhibitor molecules in H₂SO₄ solution can be described as a quasi-substitution mechanism, wherein the inhibitor molecules replace the initially adsorbed H₂SO₄ molecules. The phenomenon of adsorption can be observed in the formation of monolayers or multilayers, as described by the Freundlich adsorption isotherm equation. In order to determine the adsorption isotherm, it is necessary to have knowledge of the linear correlation between the closed surface fraction (θ) and the molar concentration (C). If the curve slope obtained by plotting $\log\{\theta/(1-\theta)C\}$ vs. θ at Equation (10) is one, then this means monolayer adsorption [36].

Plot $\log\{\theta/(1-\theta)C\}$ vs. θ of Equation (10) for the Freundlich equation gives a straight line with an R² value of 0.92 (Fig. 7). Values that are close to one suggest that the inhibitor molecule adsorption on 304SS uses the Freundlich adsorption isotherm [3,47]. Hence, the process of adsorption can occur via the creation of both monolayers and multilayers. Nevertheless, the production of a full monolayer occurred prior to the development of a multilayer. From the curve intersection, the K_{ads} value was calculated and obtained. The following equation was applied to determine the free energy of Gibbs.

$$\Delta G^\circ \text{ads} = -2.303RT\log(K_{ads} \times 55.5) \quad (11)$$

K_{ads} = a constant. The value was taken from the Freundlich equation results. The value in the experiment is 2.04. The work temperature is 27 °C, which is 300 K, and R = 8.314 J/K⁻¹ mol⁻¹.

Substitute all the values in Equation (14) and the free energy value is -11.85 kJ/Mol. A negative value for free energy signifies the spontaneity of the process. Typically, the free energy associated with adsorption falls within an intermediate range, situated between the values observed for physical adsorption (more than -20 kJ/mol), chemical adsorption (less than -40 kJ/mol), and mixed adsorption (between -20 and -40 kJ/mol). This suggests that the process can be characterized as a mixed adsorption process [48].

3.4. Electrochemical impedance spectroscopy (EIS)

The Nyquist plot is depicted in Fig. 6b. The bode plot is shown in Fig. 6c, while the corresponding findings are elaborated in Table 3. The results of the Nyquist plot of 304SS suggest that, compared to the

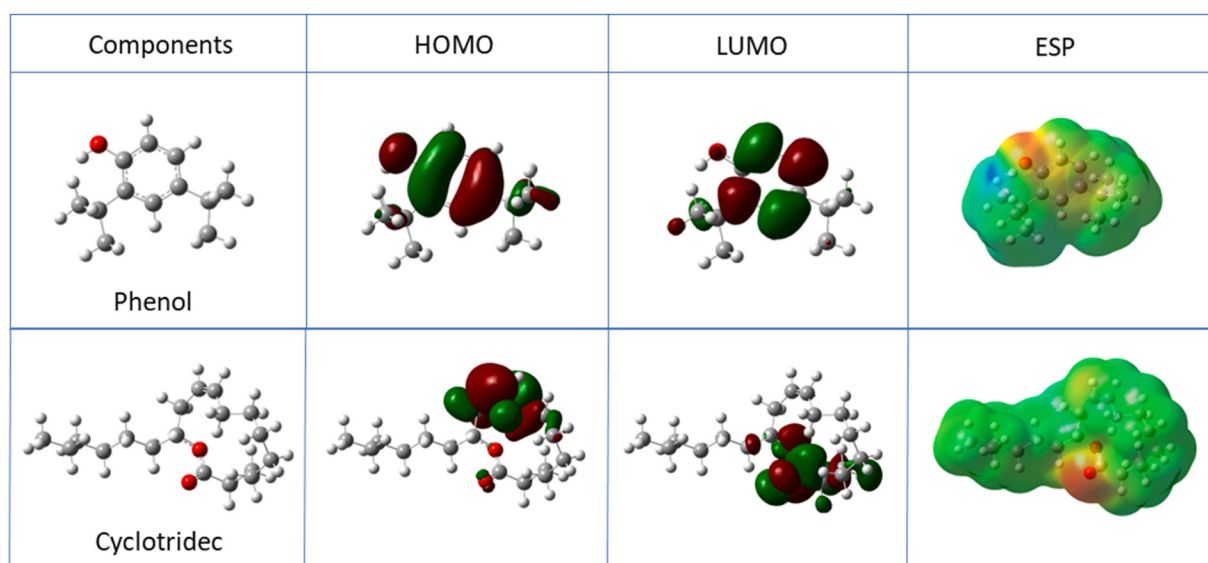


Fig. 8. HOMO, LUMO, and electrostatic potential surface (ESP) the distributions involve the components of analysis (a) phenol and (b) cyclotridec.

Table 4

Quantum chemical descriptors for phenol components in TLE.

Component	E_{HOMO} (eV)	E_{LUMO} (eV)	ΔE (eV)	I (eV)	A (eV)	η (eV)	σ	χ (eV)	μ	ω	ϵ
Phenol	−0.205	0.007	0.212	0.205	0.007	0.106	9.43	0.099	−0.099	0.046	21.73
Cyclotridec	−0.237	0.012	0.249	0.237	0.012	0.124	8.04	0.112	−0.112	0.050	20.0

solution without inhibitor, there is a significant difference in semicircular diameter capacitance due to TLE inhibitor addition to the 0.5 M H_2SO_4 solution. This indicates the existence of a one-time constant charge transfer mechanism which is represented by one capacitive loop; thus, the inhibitor can affect the corrosion reactions on the 304SS surface. The 3 g L^{-1} inhibitor concentration produced the widest diameter dimension with superior corrosion resistance capability [9]. The measurements derived from the outcomes of the EIS test include the polarization resistance (R_p), solution resistance (R_s), capacitance (Cdl), and cotangent hyperbolic (O)

The value of Cdl decreases, while R_p value raises as the inhibitor concentration increases (Table 3). The inductive loop associated with the Nyquist plot for inhibitor change occurs at low frequencies as a result of the decrease in adsorbed chemicals on the surface of the 304SS. The observed occurrence can be attributed to the degradation phenomena that takes place when the inductive loop within the EIS system ceases to function, resulting in a decline in the residual concentration. The observed consistency between the Nyquist plot's semicircular diameter trend and the change in impedance values depicted in the Bode plot, both in the presence and absence of an inhibitor, is noteworthy [10].

The results of EIS revealed the adsorption on the surface of 304SS of the TLE inhibitor film. The EIS approach is consistent with tafel polarization and hydrogen evolution. The TLE indicates inhibition of 82% at 3 g L^{-1} and R_p (788.9 Ωcm^2). The concentration of 3 g L^{-1} is considered to be the optimal inhibitor concentration since it yields the highest level of corrosion inhibition performance.

The presence of an inhibitor in the solution resulted in a discernible change in the R_p value, indicating the occurrence of polarization between the metal surface and the solution during their interaction. R_p evaluates the changes in potential resulting from comparing the applied potential with the resulting current [49]. Table 3 depicts the rise in the R_p as the inhibitor concentration is added. The highest R_p was found at 3 g L^{-1} TLE addition. The circuit model of the EIS results (Fig. 6b) shows the parallel combination between the R_p and Cdl . In Fig. 6b, the circuit model, which is identified as the R_s value, shows the solution resistance in series with R_p and Cdl . The hyperbolic cotangent constant is also visible in the circuit. The hyperbolic cotangent constant in this Nyquist plot indicates the presence of a capacitive loop that turns from the top to the bottom in the low-frequency and stable range [50,51].

3.5. HOMO-LUMO quantum analysis

The distribution of the highest occupied molecular orbitals (HOMO) and the lowest unoccupied molecular orbitals (LUMO) is depicted in Fig. 8. The ionization potential and electron affinity are associated with the energies of the highest occupied molecular orbitals, HOMO and LUMO [52].

The presence of a narrow energy gap in the inhibitor suggests a heightened level of chemical reactivity and enhanced adsorption capacity during the electron donor process within the inhibitor-metal surface contact [53]. The greater the ΔE value, the more challenging it becomes for the molecules in the inhibitor [52]. The molecules will be softer if the value gets lower. Thus, a lower ΔE value corresponds to a high electron transfer rate and an increase in inhibition, resulting in strong adsorption capabilities [46]. The distribution of HOMO and LUMO orbitals in Fig. 8 exhibits an asymmetrical pattern along the molecule chain. This indicates that the molecule is in contact with the metal substrate, but it exhibits a preference for adsorption at one end [54].

3.6. Descriptor of quantum reactivity

The findings related to the quantum reactivity index are shown in Table 4. The analysis of the HOMO and LUMO suggests that the value of −0.205 is derived from the E_{HOMO} . The idea of chemical hardness (η) provides insight into the degree of distortion or electron polarization occurring within molecules. The chemical hardness of the TLE inhibitor has been measured to be 0.140 electron volts (eV). The chemical softness (σ) of the TLE inhibitor is determined to be 7.14 electron volts (eV). The presence of a low chemical hardness (η) value and a correspondingly higher chemical softness (σ) in an inhibitor is associated with a higher level of inhibition [4]. Electrophilic index (ω) and nucleophilic (ϵ) values are: Phenol: $\omega = 0.046$, $\epsilon = 21.73$, Cyclotridec: $\omega = 0.050$, $\epsilon = 20.0$.

A higher E_{HOMO} value indicates that a molecule has a stronger ability to transfer its electrons to an acceptor (Fe), which possesses a larger quantity of unoccupied molecular orbitals [55]. This characteristic determines the inhibitor's effectiveness in preventing the oxidation (corrosion) of the metal. E_{LUMO} refers to the phenomenon where

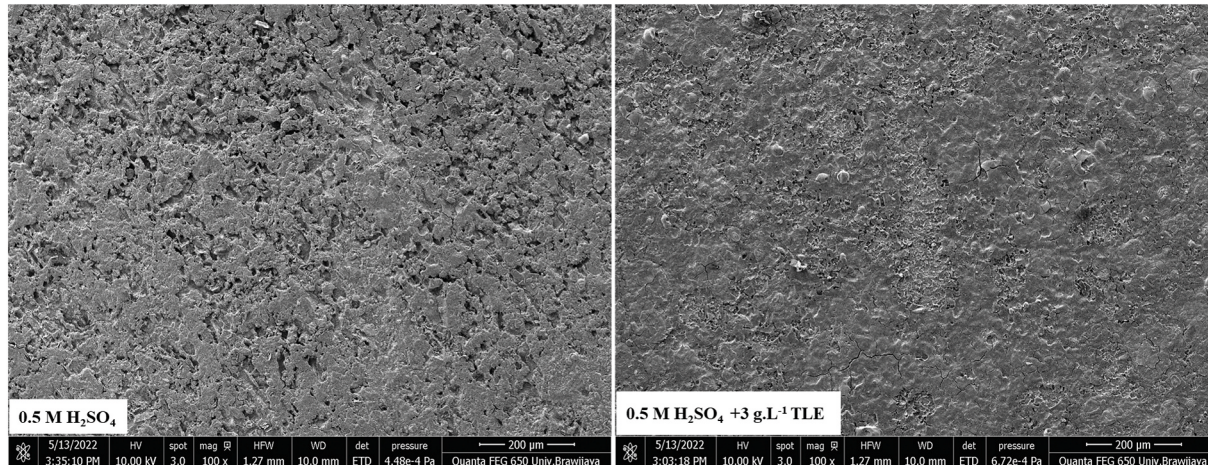


Fig. 9. SEM images of 304SS surface after a week of immersion in 0.5 M H_2SO_4 solution.

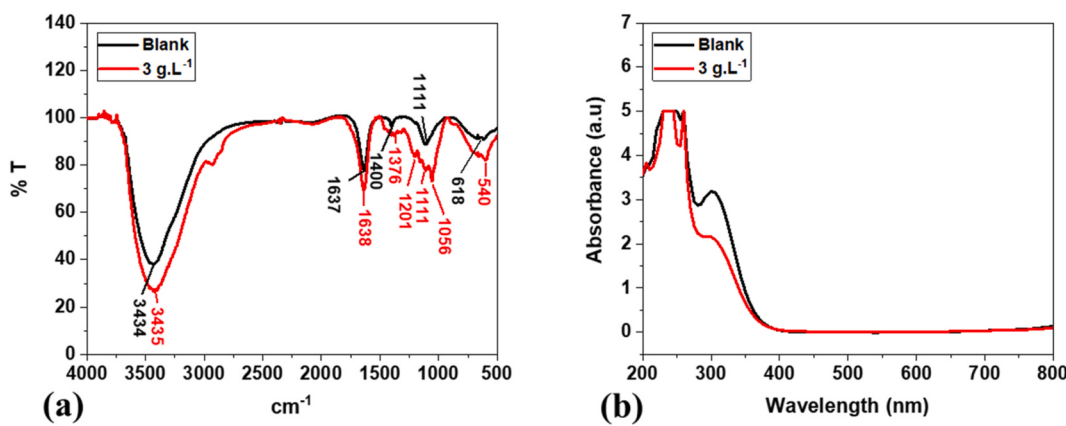


Fig. 10. a) FTIR spectra, and b) UV-Vis.

electrons have a tendency to accept full metal orbitals. The disparity between E_{HOMO} and E_{LUMO} (ΔE) is a crucial measure for assessing the reactivity of a molecule [56]. A decreased value of ΔE indicates a lower level of molecular reactivity for an inhibitor molecule. Another consequence of the disparity in energy is the propensity of a corrosion inhibitor to acquire unbound electrons from the metal. Therefore, a lower change in energy (ΔE) indicates a higher degree of adsorption of the inhibitor on the metal surface, leading to an increase in the effectiveness of inhibition. Quantum reactivity analysis shows that phenol is a more important part of how TLE sticks to 304SS in 0.5H₂SO₄.

3.7. Electrostatic potential

Fig. 8 displays the representations of the contours and electron surface, which have been visually depicted using the mapping of electrostatic potential. The red zone, denoting the electron-rich region, signifies a region with high repulsion potential [57,58]. The color blue is indicative of a partial positive potential that corresponds to an electron-deficient region, hence exhibiting a significant degree of attraction. The yellow region indicates a minor excess of electrons, whereas the green region denotes a state of neutrality. Fig. 8 illustrates that the electron density surrounding the oxygen atoms is rather low, indicating that this region is conducive to nucleophilic processes [59, 60]. The presence of a positive charge is observed in the oxygen atom, indicating the location of electrophilic activity [57,61].

3.8. Surface morphology

Fig. 9 shows SEM images of corroded 304SS surfaces in a 0.5 M H₂SO₄ solution blank or with a TLE inhibitor after a week of immersion.

Following a period of one week of complete immersion, an SEM analysis was conducted to assess the surface morphology of the 304SS. The results indicated that the specimens submerged in the TLE solution exhibited a more refined corrosion layer compared to the specimens that were not subjected to immersion in the TLE solution. When the corroded 304SS surface was put into a solution with 3 g L⁻¹ of H₂SO₄, a more compact and dense coating formed. 304SS with 3 g L⁻¹ TLE has a high R_p and is expected to exhibit a low uniform corrosion rate and a high corrosion resistance [49]. SEM reveals the surface structure of a material, including its smoothness or roughness. The specimen without an TLE inhibitor is rougher. Based on the EIS data presented, this supported SEM images.

4. FTIR and UV-VIS

Fig. 10 depicts the FTIR and UV-Vis spectra of 304SS with and without TLE inhibitor.

The FTIR and UV-Vis data show an interaction between the inhibitor

molecules that have been adsorbed onto the surface of 304SS in H₂SO₄ solution. For blank metal corrosion powder, it is observed that there are peaks at 3434 and 3435 cm⁻¹, which are strains of the O-H functional groups of alcohols. The absorption band at wavenumbers of 1637 and 1638 cm⁻¹ is seen as stretching C=O/C=N. Absorption at wavenumber of 1400 cm⁻¹ can be assumed to be C-O extended vibrations in amides of the corrosion product of 304SS [36,62]. On the steel surface with the Timoho extract inhibitor, there are four wavenumber absorptions that are not present in blank samples, namely absorption at 1376, 1201, and 1056 cm⁻¹. They are assumed to be C-N (aromatic amine), C-O (carboxylic acid), and C-O (alcohol). This proves that there is a spectrum of inhibitors adsorbed on the surface of 304SS samples, showing almost all peaks of these characteristics. Low peak intensity may indicate bond formation as well as a thin layer of inhibitor coating on the surface of the 304SS [24,63]. The IR spectra of the Timoho extract inhibitor generally exhibit anticorrosive properties due to its O heteroatoms and aromatic rings. In a 304SS specimen treated with 3 g L⁻¹, there is an indication that there are nitrogen and oxygen compounds in the functional groups of C-N (aromatic amine), C-O (carboxylic acid), and C-O (alcohol), which match the typical corrosion inhibitor structure and have been adsorbed onto 304SS. The phenol and cyclotridec compounds contain O-atoms in functional groups, O-heterocyclic rings, and the presence of electron rich multiple bonds, which meet the general characteristics of typical corrosion inhibitors. Phenols have the ability to function as chelating agents by attaching to a metal ion (Mⁿ⁺) at two specific locations on the molecule [64].

The UV-Vis spectra of 304SS in 0.5 M H₂SO₄ with and without TLE are presented in Fig. 10b. The value and the highest absorbance peak position change in the UV-Vis spectra. This means that complex compounds have been formed between the 304SS and TLE inhibitor in the solution [65,66]. At absorbance spectrum at UV-Vis, the 304SS absorbance without a TLE inhibitor is higher than that with inhibitor. This is associated with the shift in the maximum absorbance value (λ_{max}) of the complex molecule formation between the 304SS's surface and the inhibitor molecules [65].

Fig. 10b of the blank sample shows that the absorption band at 251 nm is caused by the n- σ^* and/or $\pi-\pi^*$ transition, which characterizes the carboxyl groups, esters, carbonyls, and amines of the Timoho extract inhibitor. The absorption band at around 315 nm may be ascribed to the $\pi-\pi^*$ electron transition occurring in aromatic and poly-aromatic compounds which are commonly present in conjugated molecules. The presence of double or triple bonds in molecules has been found to have advantageous effects in terms of corrosion inhibition. However, it is important to note that these bonds also contribute to an increase in toxicity. UV-Vis spectra of 304SS of both absorbance peaks show a shift, indicating the adsorption of TLE inhibitor on the surface of 304SS.

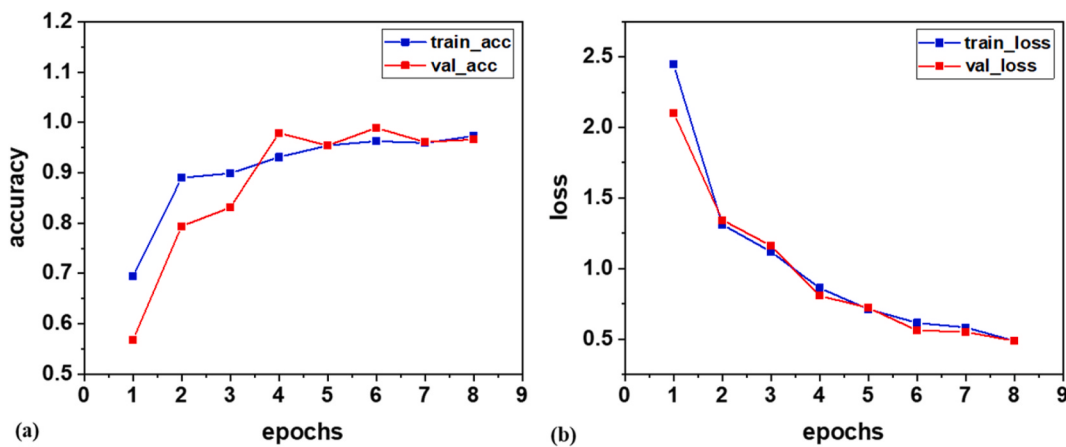


Fig. 11. a) accuracy, b) loss comparison.

		Predicted						
		1	2	3	4	5	6	Blank
Actual	1	50	0	0	0	0	0	0
	2	3	47	0	0	3	0	0
	3	0	6	43	1	0	0	0
	4	0	2	1	47	0	0	0
	5	0	0	0	0	50	0	0
	6	0	0	0	0	0	50	0
	Blank	0	0	0	0	0	0	50

Fig. 12. Confusion matrix.

4.1. Corrosion inhibition mechanism

TLE inhibitors contain the major compounds of phenol and cyclohexane. Phenol forms a protective oxide film on metal surfaces, inhibiting corrosion by preventing contact with corrosive substances. The addition of water enhances these properties, maintaining the integrity of the film. Phenol improves the corrosion resistance of 304SS by adhering well to the surface and reducing the corrosion rate. The TLE inhibitor inhibits metal corrosion by pushing the reaction at the anodic and/or cathodic sites on the surface of 304SS. The inhibition of metal corrosion involves two main processes: the suppression of anodic metal dissolution by the presence of a TLE inhibitor and the reduction of hydrogen evolution through cathodic reactions. The corrosion mechanism of 304SS in a 0.5M H₂SO₄ solution can be described as the simultaneous occurrence of hydronium ion adsorption and hydrogen gas development at the cathodic site [67,68]. At the cathode, the 304SS engages in electron competition with hydrogen ions due to the presence of an inhibitor [20].

Following the process of adsorption, the inhibitor undergoes electron transfer from the 304SS, resulting in the creation of electrically neutral molecules that function as inhibitors. Nonbonding electrons can move from heteroatoms and π electrons to the d-orbital of metal atoms on the surface with the help of neutral species. This is then followed by the creation of a coordinate bond between the metal and the adsorbed species, as has been documented in the case of several organic inhibitors [65,69]. Due to the electron-rich nature of metals, interelectronic repulsion occurs when electron transfer takes place from the d orbitals of

surface metal atoms to the orbitals of antibonding molecules. This phenomenon is commonly referred to as retro-donation. The phenomenon of mutual and retro-donation can exhibit enhanced efficacy when combined synergistically, leading to the formation of metal surface barriers that effectively impede the process of metal corrosion [65,70].

4.2. The implementation of VGG16 modelling

The results of accuracy and loss in the training process can be seen in Fig. 11.

Several metrics used to quantify the effectiveness of the model may be retrieved from the confusion matrix in Fig. 12. They include precision, recall, f1-score, and accuracy.

The model demonstrated exceptional performance, as indicated by the test results and as evidenced by its ability to predict all input accurately. The model could achieve 96% accuracy on the test set and obtain other good metrics scores. This was because the data variations were not too far from each class, which allowed the model to predict appropriately for each test.

Conclusion

1. The inhibitor addition to a 0.5 M H₂SO₄ solution led to a decrease in corrosion rates, and the potentiodynamic polarization suggested TLE as a mixed-type inhibitor.
2. The most effective inhibition efficiency was achieved with a 3 g L⁻¹ TLE inhibitor, with mixed adsorption as the primary mechanism, as determined by Freundlich adsorption isotherm analysis.
3. CNN-VGG16's prediction model achieved 96% accuracy in accurately predicting the physical changes of 304SS surface gas bubbles during the corrosion process.

In this study, electrochemical testing and gas bubbles were analyzed to determine the effectiveness of TLE inhibitor in reducing corrosion of 304SS in a 0.5 M H₂SO₄ solution. The addition of TLE inhibitor concentration caused an increase in inhibition efficiency due to the adsorption mechanism and film formation on the surface of 304SS in 0.5 M H₂SO₄. Quantum reactivity analysis revealed that phenol plays a crucial role in the adsorption of TLE to 304SS in 0.5H₂SO₄. The quantum chemistry method improved the comprehension of the adsorption of TLE inhibitor and 304SS surface in 0.5 M H₂SO₄ solution.

Declaration of competing interest

The authors declare that they have no known competing financial interests or personal relationships that could have appeared to influence the work reported in this paper.

Acknowledgement

We would like to express our gratitude to HAPKI WCU QS100 T A 2023-WCU Universitas Brawijaya, Indonesia with grant No. 2442.1/UN10/10/2023 for their financial assistance.

References

- [1] Al-Mayouf AM, Al-Suhybani AA, Al-Ameery AK. Corrosion inhibition of 304SS in sulfuric acid solutions by 2-methyl benzazole derivatives. Desalination 1998;116. [https://doi.org/10.1016/S0011-9164\(98\)00054-X](https://doi.org/10.1016/S0011-9164(98)00054-X).
- [2] Obaid AY, Ganash AA, Qusti AH, Elroby SA, Hermas AA. Corrosion inhibition of type 430 stainless steel in an acidic solution using a synthesized tetra-pyridinium ring-containing compound. Arab J Chem 2017;10. <https://doi.org/10.1016/j.arabjc.2013.03.008>.
- [3] Hermas AA, Morad MS, Wahdan MH. Effect of PgTPhPBr on the electrochemical and corrosion behaviour of 304 stainless steel in H₂SO₄ solution. J Appl Electrochem 2004;34. <https://doi.org/10.1023/B:JACH.0000005592.68605.55>.
- [4] Hooshmand Zaferani S, Sharifi M, Zareei D, Shishesaz MR. Application of eco-friendly products as corrosion inhibitors for metals in acid pickling processes - a review. J Environ Chem Eng 2013;1. <https://doi.org/10.1016/j.jece.2013.09.019>.
- [5] Ellison BT, Schmeal WR. Corrosion of steel in concentrated sulfuric acid. J Electrochim Soc 1978;125. <https://doi.org/10.1149/1.2131491>.
- [6] Francis R. The performance of stainless steels in concentrated sulphuric acid, *S t a i n l e s s S t e e l W o r l d*. 2009.
- [7] Jones S, Li Y, Coley KS, Kish JR, Ives MB. Corrosion potential oscillations of nickel-containing stainless steel in concentrated sulphuric acid: II Mechanism and kinetic modelling. Corrosion Sci 2010;52. <https://doi.org/10.1016/j.corsci.2009.09.012>.
- [8] Pracht G, Perschnick N. A material Challenge - pumps in sulphuric acid application. In: Procedia eng; 2016. <https://doi.org/10.1016/j.proeng.2016.02.101>.
- [9] Sharma S, Kumar A. Recent advances in metallic corrosion inhibition: a review. J Mol Liq 2021;322. <https://doi.org/10.1016/j.molliq.2020.114862>.
- [10] Gapsari F, Setyarini PH, Utaminingrum F, Sulaiman AM, Haidar MF, Julian TS. Melaleuca leaves extract as eco-friendly inhibitor for low carbon steel in sulfuric acid. Case Stud. Chem. Environ. Eng. 2024;9:100657. <https://doi.org/10.1016/j.csce.2024.100657>.
- [11] Sastri VS. Green corrosion inhibitors: theory and practice. <https://doi.org/10.1002/9781118015438>; 2011.
- [12] Singh WP, Bockris JOM. Toxicity issues of organic corrosion inhibitors: applications of QSAR model. In: Nace - int. Corros. Conf. Ser.; 1996.
- [13] El-Etre AY. Inhibition of aluminum corrosion using *Opuntia* extract. Corrosion Sci 2003. [https://doi.org/10.1016/S0010-938X\(03\)00066-0](https://doi.org/10.1016/S0010-938X(03)00066-0).
- [14] Oguzie EE. Corrosion inhibition of aluminium in acidic and alkaline media by *Sansevieria trifasciata* extract. Corrosion Sci 2007;49:1527–39. <https://doi.org/10.1016/j.corsci.2006.08.009>.
- [15] Ahanotu CC, Onyeachukwu IB, Solomon MM, Chikwe IS, Chikwe OB, Eziukwu CA. *Pterocarpus santalinoides* leaves extract as a sustainable and potent inhibitor for low carbon steel in a simulated pickling medium. Sustain. Chem. Pharm. 2020;15. <https://doi.org/10.1016/j.scp.2019.100196>.
- [16] Prasad D, Singh R. Natural corrosion inhibitor of renewable eco-waste for SS-410 in sulfuric acid medium : adsorption, electrochemical , and computational studies 2022;351. <https://doi.org/10.1016/j.molliq.2022.118671>.
- [17] Tan B, Fu A, Guo L, Ran Y, Xiong J, Marzouki R, Li W. Insight into anti-corrosion mechanism of *Dalbergia odorifera* leaves extract as a biodegradable inhibitor for X70 steel in sulfuric acid medium. Ind Crops Prod 2023;194:116106. <https://doi.org/10.1016/j.indcrop.2022.116106>.
- [18] Tan B, Lan W, Zhang S, Deng H, Qiang Y, Fu A, Ran Y, Xiong J, Marzouki R, Li W. Passiflora edulis Sims leaves Extract as renewable and degradable inhibitor for copper in sulfuric acid solution. Colloids Surfaces A Physicochem. Eng. Asp. 2022; 645. <https://doi.org/10.1016/j.colsurfa.2022.128892>.
- [19] Gapsari F, Setyarini PH, Kurniawan F, Ahnaf A, Anwar MS, Zuryati UK. Corrosion inhibition of weldment by nephelium lappaceum peel extract in 3.5 % NaCl solution. South Afr J Chem Eng 2022. <https://doi.org/10.1016/j.sajce.2022.06.006>.
- [20] Liao LL, Mo S, Luo HQ, Li NB. Corrosion protection for mild steel by extract from the waste of lychee fruit in HCl solution: experimental and theoretical studies. J Colloid Interface Sci 2018. <https://doi.org/10.1016/j.jcis.2018.02.071>.
- [21] Deyab MA, Mohsen Q, Guo L. *Aesculus hippocastanum* seeds extract as eco-friendly corrosion inhibitor for desalination plants: experimental and theoretical studies. J Mol Liq 2022;361. <https://doi.org/10.1016/j.molliq.2022.119594>.
- [22] Fekkar G, Younsi F, Elmsellam H, Aiboudi M, Ramdani M, Abdel-Rahman, Hammouti B, Bouyazza L. Eco-friendly chamaerops humilis l. Fruit extract corrosion inhibitor for mild steel in 1 M HCl. Int. J. Corros. Scale Inhib. 2020;9. <https://doi.org/10.17675/2305-6894-2020-9-2-4>.
- [23] Singh A, Lin Y, Ebens EE, Liu W, Pan J, Huang B, Gingko biloba fruit extract as an eco-friendly corrosion inhibitor for J55 steel in CO₂ saturated 3.5% NaCl solution. J Ind Eng Chem 2015. <https://doi.org/10.1016/j.jiec.2014.09.034>.
- [24] Hidayatullah S, Mudjib A, Nur E. Mechanics exploration and material innovation (MEMI) durio zibethinus extract performance as corrosion inhibitor in simulated seawater, vol. 1; 2024.
- [25] Olawale O, Oyawale AO, Adediran AA, Obafemi AS. Corrosion inhibition of mild steel in seawater using jatropha stem. Analele Univ. "Eftimie Murgu" Reșița; 2016. p. 228–38.
- [26] Napper AD, Bennett SP, Borowski M, Holdridge MB, Leonard MJ, Rogers EE, Duan Y, Laursen RA, Reinhold B, Shames SL. Purification and characterization of multiple forms of the pineapple-stem-derived cysteine proteinases ananain and comosain. Biochem J 1994;301(Pt 3):727–35. <https://doi.org/10.1042/bj3010727>.
- [27] Galedari SA, Mahdavi A, Azarmi F, Huang Y, McDonald A. A comprehensive review of corrosion resistance of thermally-sprayed and thermally-diffused protective coatings on steel structures. <https://doi.org/10.1007/s11666-019-00855-3>; 2019.
- [28] Fajardo S, Frankel GS. Gravimetric method for hydrogen evolution measurements on dissolving magnesium. J Electrochim Soc 2015;162. <https://doi.org/10.1149/2.0241514jes>.
- [29] Jia Z, Fu M, Zhao X, Cui Z. Intelligent identification of metal corrosion based on Corrosion-YOLOv5s. Displays 2023;76. <https://doi.org/10.1016/j.displa.2022.102367>.
- [30] Gaur A, Kishore K, Jain R, Pandey A, Singh P, Wagri NK, Roy-Chowdhury AB. A novel approach for industrial concrete defect identification based on image processing and deep convolutional neural networks. Case Stud Constr Mater 2023; 19. <https://doi.org/10.1016/j.cscm.2023.e02392>.
- [31] Abhishek A, Deb SD, Jha RK, Sinha R, Jha K. Classification of leukemia using fine tuned VGG16. In: Proc. 2023 int. Conf. Signal process. Comput. Electron. Power telecommun. IConSCEPT 2023; 2023. <https://doi.org/10.1109/IConSCEPT57958.2023.10170285>.
- [32] Andoko A, Gapsari F, Diharjo K, M R S, Siengchin S. Isolation of microcellulose from Timoho fiber using the process of delignification and maceration: evaluation of physical, chemical, structural, and thermal properties. Int J Biol Macromol 2022. <https://doi.org/10.1016/j.ijbiomac.2022.10.225>.
- [33] Gapsari F, Andoko A, Diharjo K, Sanjay MR, Siengchin S. The effectiveness of isolation and characterization nanocellulose from Timoho fiber for sustainable materials. Biomass Convers. Biorefinery 2022. <https://doi.org/10.1007/s13399-022-03672-x>.
- [34] Gapsari F, Purnowidodo A, Hidayatullah S, Suteja S. Characterization of Timoho Fiber as a reinforcement in green composite. J Mater Res Technol 2021;13. <https://doi.org/10.1016/j.jmrt.2021.05.049>.
- [35] Gapsari F, Darmadi BD, Setyarini PH, Wijaya H, Madurani KA, Juliano H, Sulaiman AM, Hidayatullah S, Tanji A, Hermawan H. Analysis of corrosion inhibition of Kleinvoglia hospita plant extract aided by quantification of hydrogen evolution using a GLCM/SVM method. Int J Hydrogen Energy 2023;48:15392–405. <https://doi.org/10.1016/j.ijhydene.2023.01.067>.
- [36] Yunita T, Putri Kusuma AW, Novita SE. Sulistijono, effect of addition tahongai leaf extract (kleinhovia hospita linn.) as organic inhibitor on 1040 AISI steel. In: IOP conf. Ser. Mater. Sci. Eng. Institute of Physics Publishing; 2019. <https://doi.org/10.1088/1757-899X/547/1/012006>.
- [37] Gapsari F, WijayaAndoko H, Suprapto A. The performance of bee wax propolis inhibitor on the Ductile Cast Iron (DCI) in saline and acidic environment. Int. Rev. Model. Simulations 2019;12. <https://doi.org/10.15866/iremos.v12i3.17085>.
- [38] Tan B, Zhang S, Cao X, Fu A, Guo L, Marzouki R, Li W. Insight into the anti-corrosion performance of two food flavors as eco-friendly and ultra-high performance inhibitors for copper in sulfuric acid medium. J Colloid Interface Sci 2022;609:838–51. <https://doi.org/10.1016/j.jcis.2021.11.085>.
- [39] Tan B, He J, Zhang S, Xu C, Chen S, Liu H, Li W. Insight into anti-corrosion nature of Betel leaves water extracts as the novel and eco-friendly inhibitors. J Colloid Interface Sci 2021;585:287–301. <https://doi.org/10.1016/j.jcis.2020.11.059>.
- [40] Doménech-Carbó A, Amparo Peiró Ronda M, Vives-Ferrández J, Duffó GS, Farina S, Teresa Doménech-Carbó M. Modeling 'dry' OCP measurements to characterize archaeological iron corrosion I: long-time transients. J Electroanal Chem 2022;913: 116210. <https://doi.org/10.1016/j.jelechem.2022.116210>.
- [41] Abd El-Fattah M, Hasan AMA, Keshawy M, El Saeed AM, Aboelenien OM. Nanocrystalline cellulose as an eco-friendly reinforcing additive to polyurethane coating for augmented anticorrosive behavior. Carbohydr Polym 2018;183. <https://doi.org/10.1016/j.carbpol.2017.12.084>.
- [42] Quariahi MA, Singh A, Singh VK, Yadav DK, Singh AK. Green approach to corrosion inhibition of mild steel in hydrochloric acid and sulphuric acid solutions by the extract of *Murraya koenigii* leaves. Mater Chem Phys 2010;122. <https://doi.org/10.1016/j.matchemphys.2010.02.066>.
- [43] Ji G, Shukla SK, Ebens EE, Prakash R. Argemone mexicana leaf extract for inhibition of mild steel corrosion in sulfuric acid solutions. Int J Electrochim Sci 2013;8.
- [44] Kurniawan F, Madurani KA. Electrochemical and optical microscopy study of red pepper seed oil corrosion inhibition by self-assembled monolayers (SAM) on 304 SS. Prog Org Coatings 2015. <https://doi.org/10.1016/j.porgcoat.2015.07.010>.
- [45] Hameed RSA, Aleid GMS, Mohammad D, Badr MM, Huwaihel B, Suliman MS, Alshammary F, Abdallah M. *Spinacia olereacea* extract as green corrosion inhibitor for carbon steel in hydrochloric. Spinacia olereacea Extract as Green Corrosion Inhibitor for Carbon Steel in Hydrochloric [1] Hameed RSA, Aleid GMS, Mohammad D, Badr MM, Huwaihel B, Suliman MS, et al. Int J Electrochim Sci 2022;17. <https://doi.org/10.20964/2022.10.31>.
- [46] Abdallah M, Altass HM, Al-Gorair AS, Al-Fahemi JH, Jahdaly BAAL, Soliman KA. Natural nutmeg oil as a green corrosion inhibitor for carbon steel in 1.0 M HCl solution: chemical, electrochemical, and computational methods. J Mol Liq 2021; 323. <https://doi.org/10.1016/j.molliq.2020.115036>.
- [47] Gapsari F, Madurani KA, Simanjuntak FM, Andoko A, Wijaya H, Kurniawan F. Corrosion inhibition of honeycomb waste extracts for 304 stainless steel in sulfuric acid solution. Materials 2019. <https://doi.org/10.3390/ma12132120>.
- [48] Chen MF, Chen Y, Jia Lim Z, Wah Wong M. Adsorption of imidazolium-based ionic liquids on the Fe(1 0 0) surface for corrosion inhibition: physisorption or

- chemisorption? *J Mol Liq* 2022;367. <https://doi.org/10.1016/j.molliq.2022.120489>.
- [49] Ferreira DL, Alves EM, de Sousa GR, Ferreira PHB, Figueiredo JMA, Leite NB, Moreto JA. Electrochemical impedance spectroscopy: basic principles and some applications. *Rev. Virtual Quim.* 2023;15. <https://doi.org/10.21577/1984-6835.20220114>.
- [50] Ostovari A, Hoseinieh SM, Peikari M, Shadizadeh SR, Hashemi SJ. Corrosion inhibition of mild steel in 1 M HCl solution by henna extract: a comparative study of the inhibition by henna and its constituents (Lawsonone, Gallic acid, α -d-Glucose and Tannic acid). *Corrosion Sci* 2009. <https://doi.org/10.1016/j.corsci.2009.05.024>.
- [51] Zhang QH, Hou BS, Li YY, Zhu GY, Liu HF, Zhang GA. Two novel chitosan derivatives as high efficient eco-friendly inhibitors for the corrosion of mild steel in acidic solution. *Corrosion Sci* 2020. <https://doi.org/10.1016/j.corsci.2019.108346>.
- [52] Behloul H, Ferkous H, Bougda N, Djellali S, Alam M, Djilani C, Sedik A, Lerari D, Jeon BH, Benguerba Y. New insights on the adsorption of Cl-Reactive Red 141 dye using activated carbon prepared from the ZnCl₂-treated waste cotton fibers: statistical physics, DFT, COSMO-RS, and AIM studies. *J Mol Liq* 2022;364. <https://doi.org/10.1016/j.molliq.2022.119956>.
- [53] En-Nyly M, Skal S, El aoufir Y, Lgaz H, Admin RJ, Alrashdi AA, Bellaouchou A, Al-Hadeethi MR, Benali O, Guedira T, Lee HS, Kaya S, Ibrahim SM. Performance evaluation and assessment of the corrosion inhibition mechanism of carbon steel in HCl medium by a new hydrazone compound: insights from experimental, DFT and first-principles DFT simulations. *Arab J Chem* 2023;16. <https://doi.org/10.1016/j.arabjc.2023.104711>.
- [54] El-Hajjaji F, Merimi I, Messali M, Obaid RJ, Salim R, Taleb M, Hammouti B. Experimental and quantum studies of newly synthesized pyridazinium derivatives on mild steel in hydrochloric acid medium. *Mater Today Proc* 2019. <https://doi.org/10.1016/j.matpr.2019.04.045>.
- [55] Li L, Zhang X, Lei J, He J, Zhang S, Pan F. Adsorption and corrosion inhibition of *Osmanthus fragrans* leaves extract on carbon steel. *Corrosion Sci* 2012. <https://doi.org/10.1016/j.corsci.2012.05.026>.
- [56] Ser CT, Žuvela P, Wong MW. Prediction of corrosion inhibition efficiency of pyridines and quinolines on an iron surface using machine learning-powered quantitative structure-property relationships. *Appl Surf Sci* 2020;512. <https://doi.org/10.1016/j.apsusc.2020.145612>.
- [57] Alvarez PE, Fiori-Bimbi MV, Neske A, Brandán SA, Gervasi CA. *Rollinia occidentalis* extract as green corrosion inhibitor for carbon steel in HCl solution. *J Ind Eng Chem* 2018;58. <https://doi.org/10.1016/j.jiec.2017.09.012>.
- [58] Berisha A. Experimental, Monte Carlo and molecular dynamic study on corrosion inhibition of mild steel by pyridine derivatives in aqueous perchloric acid. *Electrochemistry (Tokyo, Jpn)* 2020;1:188–99. <https://doi.org/10.3390/electrochem1020013>.
- [59] Haque J, Ansari KR, Srivastava V, Quraishi MA, Obot IB. Pyrimidine derivatives as novel acidizing corrosion inhibitors for N80 steel useful for petroleum industry: a combined experimental and theoretical approach. *J Ind Eng Chem* 2017;49. <https://doi.org/10.1016/j.jiec.2017.01.025>.
- [60] Bedir AG, Abd El-Raouf M, Abdel-Mawgoud S, Negm NA, El Basiony NM. Corrosion inhibition of carbon steel in hydrochloric acid solution using ethoxylated nonionic surfactants based on schiff base: electrochemical and computational investigations. *ACS Omega* 2021;6. <https://doi.org/10.1021/acsomega.0c05476>.
- [61] Chauhan DS, Mazumder MAJ, Quraishi MA, Ansari KR, Suleiman RK. Microwave-assisted synthesis of a new Piperonal-Chitosan Schiff base as a bio-inspired corrosion inhibitor for oil-well acidizing. *Int J Biol Macromol* 2020. <https://doi.org/10.1016/j.ijbiomac.2020.04.195>.
- [62] Almeida E, Pereira D, Figueiredo MO, Lobo VMM, Morcillo M. The influence of the interfacial conditions on rust conversion by phosphoric acid. *Corrosion Sci* 1997;39. [https://doi.org/10.1016/S0010-938X\(97\)00058-9](https://doi.org/10.1016/S0010-938X(97)00058-9).
- [63] Shamsheera KO, Prasad AR, Joseph A. Extended protection of mild steel in saline and acidic environment using stearic acid grafted chitosan preloaded with mesoporous-hydrophobic silica (mhSiO₂). *Surf Coating Technol* 2020;402. <https://doi.org/10.1016/j.surfcoat.2020.126350>.
- [64] Du P, Deng S, Du G, Shao D, Xu D, Li X. Synergistic inhibition effect of Mikania micrantha extract with potassium iodide on the corrosion of cold rolled steel in methanesulfonic acid solution. *Corrosion Sci* 2023;220. <https://doi.org/10.1016/j.corsci.2023.111296>.
- [65] Prasad D, Singh R, Kaya S, el Ibrahimy B. Natural corrosion inhibitor of renewable eco-waste for SS-410 in sulfuric acid medium: adsorption, electrochemical, and computational studies. *J Mol Liq* 2022;351. <https://doi.org/10.1016/j.molliq.2022.118671>.
- [66] Ma IAW, Shafaamri A, Kasi R, Zaini FN, Balakrishnan V, Subramaniam R, Arof AK. Anticorrosion properties of epoxy/nanocellulose nanocomposite coating. *Bioresources* 2017;12. <https://doi.org/10.15376/biores.12.2.2912-2929>.
- [67] Atta NF, Fekry AM, Hassaneen HM. Corrosion inhibition, hydrogen evolution and antibacterial properties of newly synthesized organic inhibitors on 316L stainless steel alloy in acid medium. *Int J Hydrogen Energy* 2011;36. <https://doi.org/10.1016/j.ijhydene.2011.02.134>.
- [68] Panossian Z, de Almeida NL, de Sousa RMF, Pimenta G de S, Marques LBS. Corrosion of carbon steel pipes and tanks by concentrated sulfuric acid: a review. *Corrosion Sci* 2012. <https://doi.org/10.1016/j.corsci.2012.01.025>.
- [69] Haldhar R, Prasad D, Bahadur I, Dagdag O, Kaya S, Verma DK, Kim SC. Investigation of plant waste as a renewable biomass source to develop efficient, economical and eco-friendly corrosion inhibitor. *J Mol Liq* 2021;335. <https://doi.org/10.1016/j.molliq.2021.116184>.
- [70] El Faydy M, Benhiba F, Warad I, Abousalem AS, About H, Kerroum Y, Jama C, Guenbour A, Lakhrissi B, Zarrouk A. Appraisal of corrosion inhibiting ability of new 5-N-((alkylamino)methyl)quinolin-8-ol analogs for C40E steel in sulfuric acid. *Int J Hydrogen Energy* 2021;46. <https://doi.org/10.1016/j.ijhydene.2021.06.205>.